Journal of Science: Advanced Materials and Devices 6 (2021) 494–500

Contents lists available at ScienceDirect

Journal of Science: Advanced Materials and Devices

journal homepage: www.elsevier.com/locate/jsamd

Original Article

# Boosting charge-transfer kinetics and cyclic stability of complementary $WO_3$—NiO electrochromic devices via $SnO_x$ interfacial layer

Kun Wang [a, c], Dong Qiu [a], Hongliang Zhang [a, *], Guoxin Chen [a], Weiping Xie [a], Kai Tao [c], Shanhu Bao [d, e], Lingyan Liang [a], Junhua Gao [a], Hongtao Cao [a, b, **]

[a] Laboratory of Advanced Nano Materials and Devices, Ningbo Institute of Materials Technology and Engineering, Chinese Academy of Sciences, Ningbo 315201, China
[b] Center of Materials Science and Optoelectronics Engineering, University of Chinese Academy of Sciences, Beijing 100049, China
[c] Institute of Inorganic Materials, School of Materials Science and Chemical Engineering, Ningbo University, Ningbo 315211, China
[d] State Key Laboratory of High Performance Ceramics and Superfine Microstructure, Shanghai Institute of Ceramics, Chinese Academy of Sciences, Shanghai 200050, China
[e] Berma Technology (Ningbo) Group Co. LTD, Ningbo 315000, China

ARTICLE INFO

*Article history:*
Received 5 March 2021
Received in revised form
31 May 2021
Accepted 4 June 2021
Available online 11 June 2021

*Keywords:*
Complementary electrochromic devices
Tungsten oxide
Tin dioxide interfacial layer
Charge-transfer

ABSTRACT

The effect of interfacial layer ($SnO_x$) on the performance of the complementary electrochromic devices (ECDs) was examined, revealing that the $SnO_x/WO_3$ bilayer cathodes could enhance the electrochromic performance, such as a superior long-term cycling stability over 10,000 cycles, a high coloration efficiency of 101.61 $cm^2$ $C^{-1}$ and a maximum transmittance modulation of 49.27%@633 nm. Moreover, compared with the single layer $WO_3$, the $SnO_x/WO_3$ bilayer exhibited improved electrochemical activities and reaction kinetics. The probable explanation is that the introduced interfacial layer can boost the double injection of ions and electrons, balance the transport of ions and electrons, and protect the electrode from degradation by serving as a buffer layer during coloration/bleaching cycles. These results further provide a valuable insight for improving the electrochromic properties of the films instead of relying on conventional methods such as nanostructural or compositional control.


## 1. Introduction

The interface between nanocrystalline/nanoporous electrochromic (EC) materials and electrolytes is crucial in determining the electrochemical and EC properties [1]. The uniqueness of nanocrystalline/nanoporous EC materials, different from the conventional dense materials, lies in the large proportion of atoms located at the interfaces [2]. The nanocrystals embedded in an amorphous matrix, as a group of multibasic oxide, have attracted much research interest in recent years [3]. Especially for electrochromic applications, this kind of material has the resistance to the volume change induced by the ion insertion/extraction. A notable example is that the electrochromic performance of undoped niobium oxide ($NbO_x$) can be greatly improved by introducing tin-doped indium oxide (ITO) nanocrystals into amorphous $NbO_x$ [3]. The intrinsic properties make nanocrystal-in-glass transition metal oxides (TMO) material an ideal candidate for EC applications [4]. The electrochromic and electrochemical properties of such nanocomposites stem from the reversible redox reactions at the interface between electrochromic materials and electrolytes, which becomes especially crucial in double injection/extraction of ions and electrons in response to the applied voltages [5]. In our previous work [6], the electrochromic mechanism for nanocrystal-in-glass $WO_3$ thin film in various electrolytes has been clarified. Also, the EC performance of amorphous $WO_3$ film can be enhanced by using the well-dispersed antimony-doped tin oxide nanoparticles [7]. In addition to the fabrication of single layer EC thin

* Corresponding author. Fax: +86 574 86688153.
** Corresponding author. Laboratory of Advanced Nano Materials and Devices, Ningbo Institute of Materials Technology and Engineering, Chinese Academy of Sciences, Ningbo, 315201, China.
*E-mail addresses:* zhanghl@nimte.ac.cn (H. Zhang), h_cao@nimte.ac.cn (H. Cao).
Peer review under responsibility of Vietnam National University, Hanoi.

https://doi.org/10.1016/j.jsamd.2021.06.001

film, considerable efforts have been undertaken to develop the bilayer thin film with the interfacial layer involved. For instance [8], $Ta_2O_5$ thin films can play a critical role as a barrier layer for the EC tungsten oxide ($WO_3$) thin film to prevent the dissolution in acidic electrolyte. Another example is that the cycle life of the $WO_3$ in aqueous $Li^+$ -based electrolytes is dramatically enhanced by the self-assembly of a protective layer on $WO_3$ [9]. A lot of interfacial materials have been explored, such as $Li_4Ti_5O_{12}$ [10], $TiO_2$ [11], $SnO_2$ [12], and so on. Among them, $SnO_2$ is relevant owing to its high conductivity. For example, $SnO_2/WO_3$ core–shell nanorods or nanowires were used in lithium-ion batteries to boost the performance [13]. In terms of electrochromism, to the best of our knowledge, $SnO_x$ has not been acted as the interfacial layer and the understanding of the function of the $SnO_x$ interfacial layer is very limited.

Herein, highly nanoporous nanocrystal-in-glass $WO_3$ cathodes with or without the $SnO_x$ interfacial layer are used to make complementary $WO_3$–NiO electrochromic devices. The main aim of the present study is to obtain a general understanding of the origins of the boosting charge-transfer kinetics and cyclic properties via $SnO_x$ interfacial layer.

## 2. Experimental

### 2.1. Preparation of thin films and assembly of electrochromic devices

The $WO_3$ thin films were deposited on the ITO-coated glass at a substrate temperature of 200 °C by electron beam evaporation technique (MUE-ECO made in ULVAC, Japan). The background pressure was reduced to less than $2.00 \times 10^{-3}$ pa. Several pure $WO_3$ particles with a diameter of ~3 mm in a tungsten crucible were bombarded by an electron beam of 10 kV in the vacuum of $2.00 \times 10^{-3}$ pa. The deposition rate and thickness of thin films were 0.10 nm/s and 450 nm, respectively. Subsequently, the $SnO_x$ ultrathin layers (thickness: ~5 nm determined by a quartz-crystal film-thickness monitor, background pressure: $2.00 \times 10^{-3}$ pa) were *in situ* grown on the $WO_3$ thin films via several $SnO_2$ particles, which ensures the high-quality contact and the excellent adherence between $SnO_x$ and $WO_3$. Similarly, the NiO thin films were deposited on the ITO-coated glass at room temperature by electron beam evaporation technique from several NiO particles (deposition rate and thickness of thin films were 0.10 nm/s and 200 nm in the vacuum of $2.00 \times 10^{-3}$ pa). The as-deposited NiO thin films were annealed in air at the temperature of 300 °C for 1 h, and then cooled down naturally. The complementary ECDs with ITO/$WO_3$/$SnO_x$/$Li^+$-based electrolyte/NiO/ITO and ITO/$WO_3$/$Li^+$-based electrolyte/NiO/ITO configurations were assembled by placing $Li^+$-based electrolytes (0.10 M $LiClO_4$ dissolved into propylene carbonate) between two films in the vacuum filling process, similar to the previous report [14].

### 2.2. Characterization

The structure and morphology were analyzed by X-ray diffraction (XRD, Bruker D8 Advance using Cu-Kα ($\lambda = 0.154178$ nm) radiation and a theta-2theta configuration), X-ray photoelectron spectra (XPS) (AXIS UTLTRA DLD) using Al Kα (1486.6 eV) radiation as an X-ray source with a voltage of 15 kV and a power of 120 W at a pressure of ~$5 \times 10^{-9}$ Torr, and high-resolution transmission electron microscopy (HRTEM, JEOL2100) and field-emission scanning electron microscopy (FESEM, S4800). *In situ* transmittance spectra were obtained via UV-VIS-IR spectroscopy (Perkin–Elmer Lambda 950) and electrochemical workstation (CHI660D, Chenhua, Shanghai). Electrochemical measurements were conducted in a three-electrode cell. A platinum sheet and KCl saturated $Hg/HgCl_2$ were used as counter electrode and reference electrode, respectively. 0.10 M $LiClO_4$ dissolved into propylene carbonate (PC) was employed as an electrolyte of the ECDs. The chronoamperometry, chronocoulometry and cyclic voltammetry measurements were performed by applying voltage between −1.00 V and +1.00 V. The electrochemical impedance spectra (EIS) were measured on an electrochemical workstation (Zennium, IM6) with AC voltage amplitude of 100 mV in the frequency range from 100 mHz to 100 kHz.

## 3. Results and discussion

### 3.1. Electrochromic performance of the complementary devices

Fig. 1a and b respectively show the *ex-situ* and *in-situ* optical transmittance spectra of the fabricated devices with or without using the $SnO_x$ interfacial layer. The maximal transmittance modulation (ΔT, coloration/bleaching at 633 nm) is estimated to be 35.00% and 49.27% for the ECD without and with the $SnO_x$ interfacial layer, respectively. Moreover, ΔT determined by *in-situ* optical transmittance spectra at a −1.50 V/+1.60 V voltage for 45 s/45 s is obtained to be 47.80% and 41.60% for the ECD without and with the $SnO_x$ interfacial layer, respectively. The colored/bleached response time (the time required to reach 90% of the transmittance change between bleached and colored state [15]) is estimated to be respectively about 33 s/6 s and 17/6 s for the ECDs without and with the $SnO_x$ interfacial layer (Figure S1d), indicating that higher transmittance modulation and the faster colored response are ascribed to the addition of $SnO_x$ interfacial layer. Generally speaking, the shorter response time is partly dependent on the higher concentration of the cation ions [16]. Therefore, it is reasonable that the response time for 0.1 M $Li^+$-based electrolyte is lower than that of 0.5 M or 1.0 M $Li^+$-based electrolyte reported previously [17]. Coloration efficiency (η) of the ECD using $SnO_x$ interfacial layer is 101.61 $cm^2\ C^{-1}$, better than that (65.11 $cm^2\ C^{-1}$) of the counterpart (Fig. 1c and Figure S1a), also higher than the previous report (90 $cm^2\ C^{-1}$) [18]. The device with the $SnO_x$ layer exhibits good stability, as reflected by the almost coincident CV curves in the potential region from −1.50 V to +1.60 V at a scan rate of 50 mV/s within 100 cycles (Fig. 1d). Figure S1b and Fig. 1e respectively presents a series of relatively symmetrical galvanostatic charge/discharge curves for the devices with and without the $SnO_x$ interfacial layer at various current densities ranging from 0.10 mA $cm^{-2}$ to 0.18 mA $cm^{-2}$, suggesting that the reversible redox reaction is involved [19]. The capacitance retention ratio after 10,000 cycles is respective to be 124.03% and 103.57% for the ECDs without and with the $SnO_x$ interfacial layer, as illustrated in Fig. 1f. Specifically, the cyclic retention of more than 100% can be attributed to a continuous activation at the active interface [20]. The substantial increase of capacitance retention ratio for the ECDs without the interfacial layer is probably due to more contact of $WO_3$ with the electrolyte [21]. Moreover, the optical modulation for the ECDs with the $SnO_x$ interfacial layer is enhanced from the initial 49.27% (at $\lambda = 633$ nm) to 54.85% at the 10000th cycle (Figure S1c). The improved optical modulation can be due to the increased charge density exchange of NiO thin films with continuous cycles, which leads to more nickel atoms involved in the electrochromic reaction, as reported previously [22,23]. The optical contrast retention after 10,000 cycles is calculated to be 111.33% for the ECDs with the $SnO_x$ interfacial layer, which is corresponding with the capacitance retention. In comparison, the usage of $SnO_x$ layer is believed to have the protective effect on the $WO_3$ thin films. The dissimilar EC performance and cyclic properties indicate that $SnO_x$ interfacial layer controls charge-transfer kinetics and intercalation/

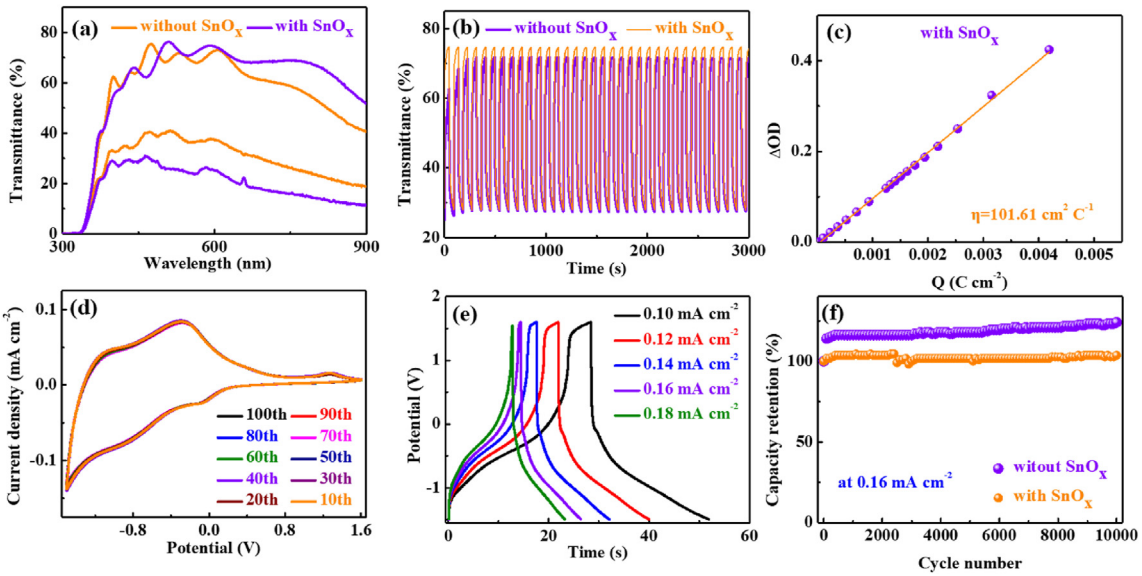


**Fig. 1.** (a) *Ex situ* transmittance spectra and (b) *in situ* time-dependent optical transmittance spectra at $\lambda_{633\ nm}$ of the $WO_3$—NiO ECD and $WO_3/SnO_x$-NiO ECD. (c) Plots of *in situ* optical density variation as a function of charge density at $\lambda_{633\ nm}$, (d) cyclic voltammograms and (e) GCD curves for the complementary $WO_3/SnO_x$-NiO ECD. (f) Cyclic performance for the $WO_3$—NiO ECD and $WO_3/SnO_x$-NiO ECD.

deintercalation processes, which subsequently affects the electrochemical activities. To support our anticipation, the electrochromic and electrochemical performance of $WO_3$ and $SnO_x/WO_3$ cathodes in $Li^+$-based electrolyte will be discussed in the following.

### 3.2. XPS of the thin films

In order to investigate the chemical state evolution of the $SnO_x$, the valence states of Sn are quantitatively analyzed via XPS spectra. High-resolution spectra of Sn in the $WO_3/SnO_x$ electrode are given in Fig. 2a and b, corresponding to the colored and bleached state, respectively. The Sn 3d signal (Fig. 2a) is consisted of three components of 485.17, 486.95 and 487.01 eV, which could be ascribed to Sn(0), Sn(II), and Sn(IV) respectively. The ratio of $Sn^0/Sn^{2+}/Sn^{4+}$ is calculated to be 1.12%/77.86%/21.02%, confirming the formation of metallic Sn and SnO by reducing a part of $SnO_2$, as stated previously [24]. In the bleached state, the Sn 3d signal has two components centered at 485.08 and 487.01 eV, corresponding to Sn(0) and Sn(IV), respectively. The concentration ratio of $Sn^0$ and $Sn^{4+}$ is respective to be 4.33% and 95.67%, indicating that more metallic Sn component is formed in the bleaching process [25]:

$$Sn + xLi^+ + xe^- \leftrightarrow Li_xSn \quad (1)$$

which contributes to the reversibility of the ECDs.

### 3.3. Electrochemical performance of the thin films

The cyclic voltammetry curves determined by the electrochemical measurements in the three-electrode system for the $WO_3$ thin film are shown in Fig. 3a. It can be seen that the peak values are increased accordingly with the scan rate. For the sake of better conductivity of $SnO_x$, the peak value at the same scan rate of the $WO_3$ thin film with the interfacial layer is larger than that of the counterpart. The switching speed of electrochromic devices is essentially dependent on the ion diffusion coefficient and ion diffusion distance [26]. As illustrated in Fig. 3b, the diffusion coefficient (D, the calculation is described in the Supplementary Material S3) is respective to be $9.40 \times 10^{-10}$ $cm^2$ $s^{-1}$ and $2.59 \times 10^{-8}$ $cm^2$ $s^{-1}$ for the $WO_3$ thin film without and with the $SnO_x$ in 0.1 M PC-$LiClO_4$, and the later one is prominently larger than the values ($10^{-10}$–$10^{-12}$ $cm^2$ $s^{-1}$) in the previous report [27]. On one side, such large values are attributed to the nanocrystal embedded amorphous phase (Supplementary Material S2) [4,27]. On the other, the diffusion coefficient is influenced by the steric resistance associated with ionic radius and electrostatic forces coupled with the charge of guest ions [28]. Compared with the $WO_3$

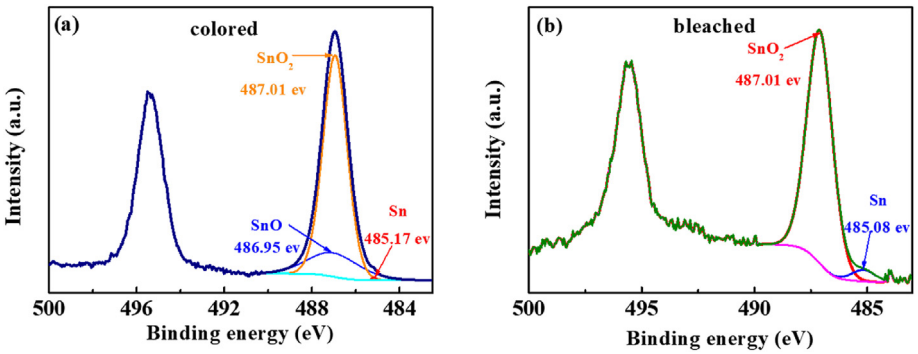


**Fig. 2.** XPS spectra of Sn 3d5 for the (a) colored and (b) bleached $WO_3$ thin films with the $SnO_x$ interfacial layer.

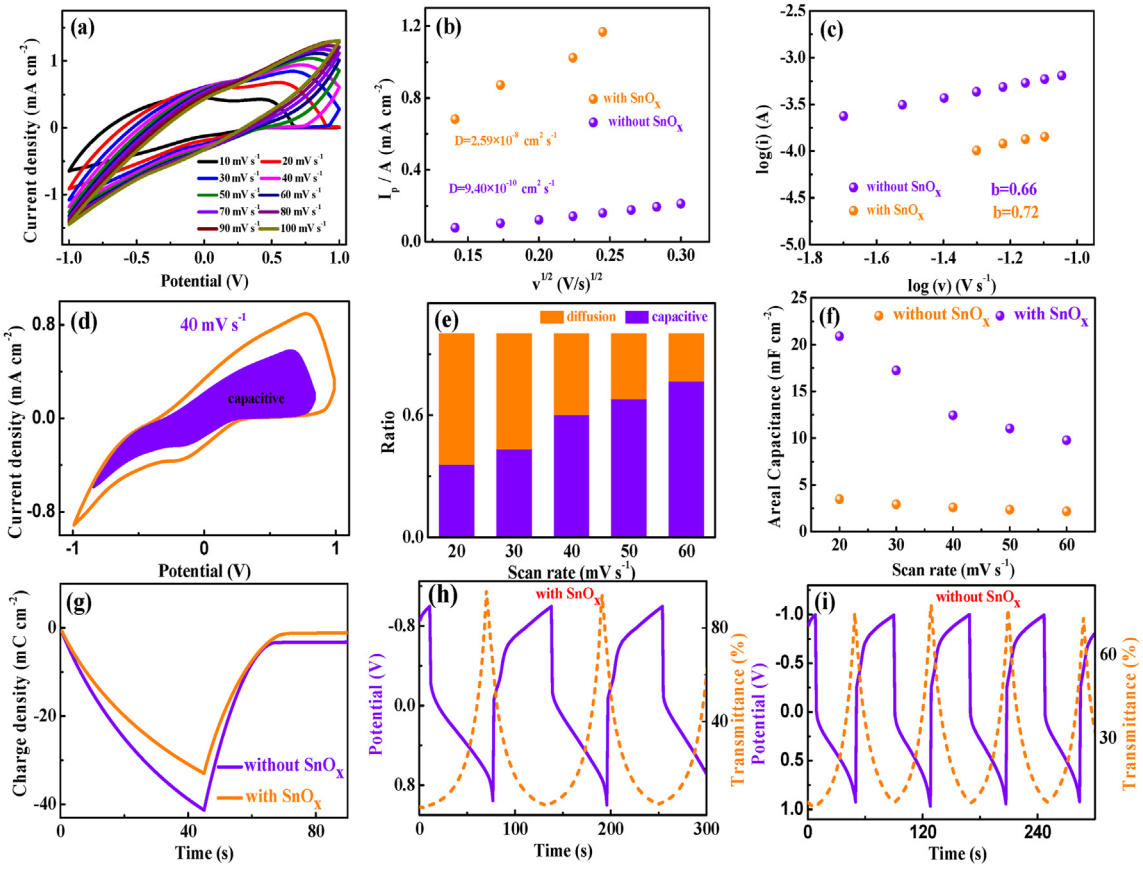


**Fig. 3.** CV profiles at various scan rates for the $WO_3$@$SnO_x$ thin films. (b) Dependence of the peak current densities ($I_p$) versus the square root of scan rate ($v^{1/2}$) and (c) power law dependence of the peak current versus the scan rate for the $WO_3$ and $WO_3$@$SnO_x$ thin films. (d) The separation of capacitance and diffusion current densities at a scan rate of 40 mV $S^{-1}$ and (e) separation of contributions from capacitive and diffusion-controlled process as a function of processes at different scan rates for the $WO_3$@$SnO_x$ thin film. (f) The areal capacitance of the $WO_3$ and $WO_3$@$SnO_x$ thin films at different scan rates. (g) Charge density of the $WO_3$ and $WO_3$@$SnO_x$ thin films. GCDs and corresponding *in situ* time-dependent optical transmittance spectra of (h) the $WO_3$@$SnO_x$ and (i) the $WO_3$ thin films in the charged and discharged state.

single layer, the larger diffusion coefficient of the $SnO_x$/$WO_3$ bilayer cathode is owing to the dissolution blockage of tungsten-containing species and higher interface conductivity. In order to evaluate the electrochemical behaviors, b value can be calculated from a relationship between the peak current (i) and scan rate (v) according to the following equation: [29].

$$i = av^b \tag{2}$$

where both a and b are adjustable values. The peak current (i) obeys a law power in response to the scan rate ($v$), and the slope of log(i) versus log ($v$) represents b. The b value of 0.5 and 1 indicates semi-infinite linear diffusion and surface-controlled (capacitive) electrochemical reaction, respectively [30]. Fig. 3c displays the power law dependence of the peak current versus the scan rate. The b value of the $WO_3$ thin film without and with the $SnO_x$ interfacial layer is calculated to be 0.66 and 0.72, respectively, suggesting that the current depends on both semi-infinite linear diffusion and capacitive-controlled behavior [31].

For interpreting the effect of the interfacial layer, the surface-capacitive ($k_1v$) and diffusion-controlled ratio ($k_2v^{\frac{1}{2}}$) are quantitatively distinguished using the follow equation [32]:

$$i(V) = k_1v + k_2v^{\frac{1}{2}} \tag{3}$$

where $i$ represents a current at a certain potential of V, and $v$ is the scan rate. As illustrated in Fig. 3d, the capacitive contribution of the $SnO_x$/$WO_3$ bilayer is 60.24% of the total capacity at a scan rate of 40 mV $s^{-1}$, suggesting that the pseudocapacitive contribution is dominant. Furthermore, the surface-capacitive section is increased from 0.30 to 0.77 and from 012 to 0.20 as the scan rates increase from 20 mV $s^{-1}$ to 60 mV $s^{-1}$ for the $WO_3$ thin film with (Fig. 3e) and without (Figure S3b) $SnO_x$, respectively. The more capacitive contribution by introducing the $SnO_x$ interfacial layer at the same scan rate is in favor of good cycling stability [33]. In order to further analyze the effect of $SnO_x$ on the electrochemical properties, the areal capacitance was calculated by the CV curves at different scan rates (Fig. 3f). The areal capacitance of $SnO_x$/$WO_3$ (for detail, please refer to S4 in the Supporting Information) is always higher than that of single $WO_3$ at whatever scan rates, manifesting enhanced capacitive performance by addition of $SnO_x$ interface [34]. It can be attributed to that $SnO_x$ boosts the electrical conductivity and contributes the redox-based pseudocapacitance via participating in the redox process. Besides, the inserted/extracted charges during the colored and bleached processes can be obtained by a chronocoulometry method, which is conducted under a square-wave voltage of −1.0 V and +1.0 V with a pulse width of 45 s. The reversibility of films can be estimated from the following equation [35]:

$$\text{Reversibility} = \frac{Q_{ex}}{Q_{in}} \times 100\% \tag{4}$$

where $Q_{ex}$ is extracted charge and $Q_{in}$ the inserted charge. Depending on Fig. 3g, the reversibility is increased from 94.17% to

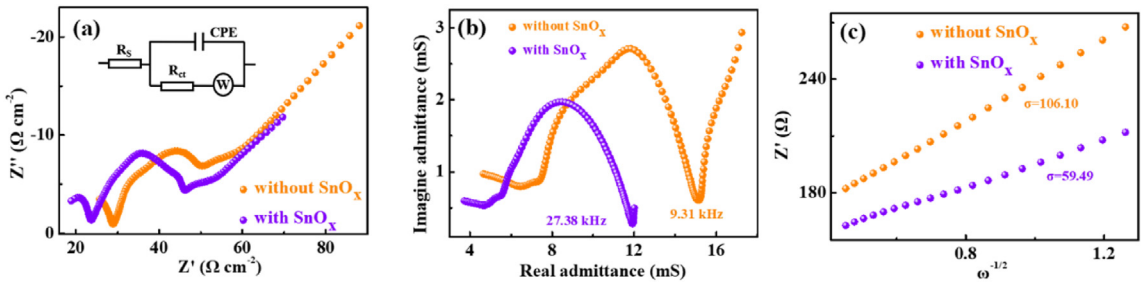


**Fig. 4.** (a) Nyquist plots, (b) admittance plots and (c) the real impedance (Z′) versus angular frequency ($\omega = 2\pi f$) dependency plots in the low-frequency region for the $WO_3$ thin film without and with the $SnO_x$ layer.

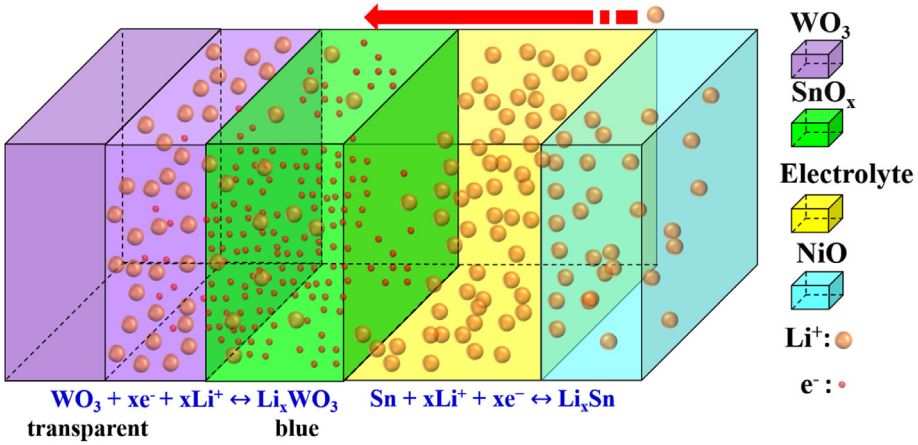


**Fig. 5.** A schematic illustration of the operation for $WO_3/SnO_x$-NiO ECD in the colored state.

98.66%, indicating that addition of $SnO_x$ enhances the reversibility. Fig. 3h and i exhibit the reversible transient transmittance corresponding to the GCD curve at 1 mA cm$^{-2}$, demonstrating the one-to-one relation between the transmittance and the potential. Thus, the real-time stored energy stage can be visually monitored by the color changing, in a good agreement with the previous report [36].

### 3.4. Electrochemical impedance spectra

The Nyquist plots in the frequency region ranging from 100 mHz to 100 kHz are shown in Fig. 4a. The EIS measurement is characterized by the Randles equal circuit model, as displayed in the inset of Fig. 4a. $R_s$ and $R_{ct}$ respectively represents the internal resistance and the interfacial charge-transfer resistance [37], which are estimated based on the impedance spectra. The observed decrease in $R_s$ and $R_{ct}$, as a hint for improved electrochemical activity and reaction kinetics, could be mainly attributed to the synergistic effect of the easier charge transfer at the electrode/electrolyte interface and the high intrinsic conductivity for $SnO_x$ [13]. The knee frequency is estimated respectively to be 9.31 kHz and 27.38 kHz for the $WO_3$ thin film without and with the $SnO_x$ layer (Fig. 4b), manifesting prompt electrochemical response when using the interfacial layer [38]. Fig. 4c presents the relationship between real resistance (Z′) and the angular frequency ($\omega = 2\pi f$). Based on Z′ and ω, the $Li^+$ diffusion coefficient (D) can be calculated by [39]:

$$Z' = R_s + R_{CT} + \sigma\omega^{-1/2},\ D = 0.5\left(\frac{RT}{An^2F^2C\sigma}\right)^2 \quad (5)$$

where σ refers to the Warburg coefficient. R, T, A, n, F and C represent the gas constant, absolute temperature, surface area for electrode, number of transfer electron, Faraday constant and ion concentration, respectively. The $Li^+$ diffusion coefficient is calculated to be $3.42 \times 10^{-11}$ cm$^2$ s$^{-1}$ and $2.59 \times 10^{-8}$ cm$^2$ s$^{-1}$ for the $WO_3$ thin film without and with the $SnO_x$, respectively, almost identical to those obtained by the cyclic voltammetry method. Based on EIS analysis, the introduction of $SnO_x$ enables the formation of a free channel in favor of ion transfer, similar to the $WO_3$@$SnO_x$ core–shell nanowire arrays [13].

### 3.5. Discussion on the effect of the $SnO_x$

The origins of boosting charge-transfer kinetics and cycling stability of complementary $WO_3$–NiO electrochromic devices via $SnO_x$ interfacial layer can be explained in Fig. 5. On one hand, a possible explanation for faster charge-transfer kinetics is that higher intrinsic conductivity of the $SnO_x$ than that of $WO_3$, resulting in small interfacial charge-transfer resistance. On the other, the introduced $SnO_x$ as a buffer layer could avoid the direct contact between $WO_3$ and the electrolyte. Based on the aforementioned XPS results, the valence state change in $SnO_x$ suggests that it is associated with reversible electrochemical processes. Therefore, the bilayer structure is applied to improve the reversibility and protect the electrode from degradation. Besides, based on the contrast summarized in Table S1, it can be observed that the prepared ECDs in this study possess more competitive cyclic stability (10,000 cycles), optical contrast retention (111.33%) and capacitance retention (103.57%) via $SnO_x$ interfacial layer than those reported previously, indicating that the $SnO_x$ layer seems to play an important role in charge-transfer kinetics and the interfacial intercalation/deintercalation processes.

## 4. Conclusion

We have demonstrated that enhancement of charge-transfer kinetics and cyclic stability can be achieved for complementary $WO_3$–NiO electrochromic devices by incorporating a thin $SnO_x$ (~5 nm) interfacial layer, resulting in shorter colored response time (17s), competitive cyclic stability (10,000 cycles) and capacitance retention (103.57%). The higher diffusion coefficient and smaller $R_{ct}$ of $WO_3$ films with the interfacial layer could be attributed to the synergistic effect of the easier charge transfer at the electrode/electrolyte interface and the high intrinsic conductivity of $SnO_x$, which decreases interfacial charge-transfer barrier and the internal resistance, balances the transport of ions and electrons, and improves cyclic stability and reversibility finally. Most importantly, the introduction of $SnO_x$ could highlight the capacitive contribution, causing a higher optical modulation and coloration efficiency, better capacitance retention and well-performed optical modulation reversibility of ECDs. Therefore, introducing a proper buffer layer between the EC material and electrolyte is a promising strategy for boosting charge-transfer kinetics and cyclic stability of electrochemical and electrochromic devices.

## Declaration of competing interest

The authors declare that they have no known competing financial interests or personal relationships that could have appeared to influence the work reported in this paper.

## Acknowledgements

This project is supported by the National Natural Science Foundation of China (61974148), and Ningbo Science and Technology Innovation 2025 Major Special Project (2020Z002).

## Appendix A. Supplementary data

Supplementary data to this article can be found online at https://doi.org/10.1016/j.jsamd.2021.06.001.

## References

[1] K.R. Reyes-Gil, Z.D. Stephens, V. Stavila, D.B. Robinson, Composite $WO_3/TiO_2$ nanostructures for high electrochromic activity, ACS Appl. Mater. Interfaces 7 (2015) 2202–2213.
[2] S.H. Lee, R. Deshpande, P.A. Parilla, K.M. Jones, B. To, A.H. Mahan, A.C. Dillon, Crystalline $WO_3$ nanoparticles for highly improved electrochromic applications, Adv. Mater. 18 (2006) 763–766.
[3] A. Llordes, G. Garcia, J. Gazquez, D.J. Milliron, Tunable near-infrared and visible-light transmittance in nanocrystal-in-glass composites, Nature 500 (2013) 323–326.
[4] S. Wang, K. Dou, Y. Zou, Y. Dong, J. Li, D. Ju, H. Zeng, Assembling tungsten oxide hydrate nanocrystal colloids formed by laser ablation in liquid into fast-response electrochromic films, J. Colloid Interface Sci. 489 (2017) 85–91.
[5] S. Masi, R. Mastria, R. Scarfiello, S. Carallo, C. Nobile, S. Gambino, T. Sibillano, C. Giannini, S. Colella, A. Listorti, P.D. Cozzoli, A. Rizzo, Room-temperature processed films of colloidal carved rod-shaped nanocrystals of reduced tungsten oxide as interlayers for perovskite solar cells, Phys. Chem. Chem. Phys. 20 (2018) 11396–11404.
[6] D. Qiu, H. Ji, X. Zhang, H. Zhang, H. Cao, G. Chen, T. Tian, Z. Chen, X. Guo, L. Liang, J. Gao, F. Zhuge, Electrochromism of nanocrystal-in-glass tungsten oxide thin films under various conduction cations, Inorg. Chem. 58 (2019) 2089–2098.
[7] K.-H. Kim, B.-R. Koo, H.-J. Ahn, Effects of Sb-doped $SnO_2$–$WO_3$ nanocomposite on electrochromic performance, Ceram. Int. 45 (2019) 15990–15995.
[8] Y. Nah, Effects of tantalum oxide films on stability and optical memory in electrochromic tungsten oxide films, Solid State Ionics 165 (2003) 229–233.
[9] E. Hopmann, A.Y. Elezzabi, Electrochemical stability enhancement of electrochromic tungsten oxide by self-assembly of a phosphonate protection layer, ACS Appl. Mater. Interfaces 12 (2020) 1930–1936.
[10] K.T. Kim, C.Y. Yu, C.S. Yoon, S.J. Kim, Y.K. Sun, S.T. Myung, Carbon-coated Li4Ti5O12 nanowires showing high rate capability as an anode material for rechargeable sodium batteries, Nano Energy 12 (2015) 725–734.
[11] S.M. Oh, J.Y. Hwang, C.S. Yoon, J. Lu, K. Amine, I. Belharouak, Y.K. Sun, High electrochemical performances of microsphere C-TiO2 anode for sodium-ion battery, ACS Appl. Mater. Interfaces 6 (2014) 11295–11301.
[12] J. Liang, W. Wei, D. Zhong, Q. Yang, L. Li, L. Guo, One-step in situ synthesis of $SnO_2$/graphene nanocomposites and its application as an anode material for Li-ion batteries, ACS Appl. Mater. Interfaces 4 (2012) 454–459.
[13] L. Gao, F. Qu, X. Wu, Hierarchical $WO_3$@$SnO_2$ core–shell nanowire arrays on carbon cloth: a new class of anode for high-performance lithium-ion batteries, J. Mater. Chem. A 2 (2014) 7367–7372.
[14] C. Xu, C. Ma, X. Kong, M. Taya, Vacuum filling process for electrolyte in enhancing electrochromic polymer window assembly, Polym. Adv. Technol. 20 (2009) 178–182.
[15] Y.D. Shi, M.J. Sun, Y. Zhang, J.W. Cui, Y. Wang, X. Shu, Y.Q. Qin, H.H. Tan, J.Q. Liu, Y.C. Wu, Structure modulated amorphous/crystalline $WO_3$ nanoporous arrays with superior electrochromic energy storage performance, Sol. Energy Mater. Sol. Cells 212 (2020) 10.
[16] B.B. Xu, L. Xu, G.G. Gao, W.H. Guo, S.P. Liu, Effects of film structure on electrochromic properties of the multilayer films containing polyoxometalates, J. Colloid Interface Sci. 330 (2009) 408–414.
[17] D.S. Dalavi, R.S. Devan, R.A. Patil, R.S. Patil, Y.-R. Ma, S.B. Sadale, I. Kim, J.-H. Kim, P.S. Patil, Efficient electrochromic performance of nanoparticulate $WO_3$ thin films, J. Mater. Chem. C 1 (2013) 3722–3728.
[18] P.-W. Chen, C.-T. Chang, T.-F. Ko, S.-C. Hsu, K.-D. Li, J.-Y. Wu, Fast response of complementary electrochromic device based on $WO_3$/NiO electrodes, Sci. Rep. 10 (2020).
[19] S. Zhou, C. Hao, J. Wang, X. Wang, H. Gao, Metal-organic framework templated synthesis of porous $NiCo_2O_4/ZnCo_2O_4/CO_3O_4$ hollow polyhedral nanocages and their enhanced pseudocapacitive properties, Chem. Eng. J. 351 (2018) 74–84.
[20] H. Chen, M. Zhou, Z. Wang, S.Y. Zhao, S.Y. Guan, Rich nitrogen-doped ordered mesoporous phenolic resin-based carbon for supercapacitors, Electrochim. Acta 148 (2014) 187–194.
[21] Y. Zhou, S. Ko, C.W. Lee, S.G. Pyo, S.-K. Kim, S. Yoon, Enhanced charge storage by optimization of pore structure in nanocomposite between ordered mesoporous carbon and nanosized $WO_{3-x}$, J. Power Sources 244 (2013) 777–782.
[22] R.T. Wen, G.A. Niklasson, C.G. Granqvist, Strongly improved electrochemical cycling durability by adding iridium to electrochromic nickel oxide films, ACS Appl. Mater. Interfaces 7 (2015) 9319–9322.
[23] R.T. Wen, C.G. Granqvist, G.A. Niklasson, Anodic electrochromism for energy-efficient windows: cation/anion-based surface processes and effects of crystal facets in nickel oxide thin films, Adv. Funct. Mater. 25 (2015) 3359–3370.
[24] N. Mohri, B. Oschmann, N. Laszczynski, F. Mueller, J. von Zamory, M.N. Tahir, S. Passerini, R. Zentel, W. Tremel, Synthesis and characterization of carbon coated sponge-like tin oxide ($SnO_x$) films and their application as electrode materials in lithium-ion batteries, J. Mater. Chem. A 4 (2016) 612–619.
[25] J.S. Chen, X.W. Lou, $SnO_2$-Based nanomaterials: synthesis and application in lithium-ion batteries, Small 9 (2013) 1877–1893.
[26] S. Zhang, S. Cao, T. Zhang, J.Y. Lee, Plasmonic oxygen-deficient $TiO_{2-x}$ nanocrystals for dual-band electrochromic smart windows with efficient energy recycling, Adv. Mater. (2020) 2004686.
[27] G. Garciabelmonte, V. Vikhrenko, J. Garciacanadas, J. Bisquert, Interpretation of variations of jump diffusion coefficient of lithium intercalated into amorphous $WO_3$ electrochromic films, Solid State Ionics 170 (2004) 123–127.
[28] R. Li, K. Li, G. Wang, L. Li, Q. Zhang, J. Yan, Y. Chen, Q. Zhang, C. Hou, Y. Li, H. Wang, Ion-transport design for high-performance $Na^+$-Based electrochromics, ACS Nano 12 (2018) 3759–3768.
[29] Z. Tong, N. Li, H. Lv, Y. Tian, H. Qu, X. Zhang, J. Zhao, Y. Li, Annealing synthesis of coralline $V_2O_5$ nanorod architecture for multicolor energy-efficient electrochromic device, Sol. Energy Mater. Sol. Cell. 146 (2016) 135–143.
[30] J.B. Mitchell, W.C. Lo, A. Genc, J. LeBeau, V. Augustyn, Transition from battery to pseudocapacitor behavior via structural water in tungsten oxide, Chem. Mater. 29 (2017) 3928–3937.
[31] R. Govindan, X.-J. Hong, P. Sathishkumar, Y.-P. Cai, F.L. Gu, Construction of metal-organic framework-derived $CeO_2$/C integrated $MoS_2$ hybrid for high-performance asymmetric supercapacitor, Electrochim. Acta 353 (2020).
[32] X. Zhang, J. Zhang, S. Kong, K. Zhu, J. Yan, K. Ye, G. Wang, K. Cheng, L. Zhou, D. Cao, A novel calendula-like $MnNb_2O_6$ anchored on graphene sheet as high-performance intercalation pseudocapacitive anode for lithium-ion capacitors, J. Mater. Chem. A 7 (2019) 2855–2863.
[33] Z. Luo, L. Liu, X. Yang, X. Luo, P. Bi, Z. Fu, A. Pang, W. Li, Y. Yi, Revealing the charge storage mechanism of nickel oxide electrochromic supercapacitors, ACS Appl. Mater. Interfaces 12 (2020) 39098–39107.
[34] T. Zhai, F. Wang, M. Yu, S. Xie, C. Liang, C. Li, F. Xiao, R. Tang, Q. Wu, X. Lu, Y. Tong, 3D MnO2-graphene composites with large areal capacitance for high-performance asymmetric supercapacitors, Nanoscale 5 (2013) 6790–6796.

[35] K.L. Zhou, H. Wang, Y.Z. Zhang, J.B. Liu, H. Yan, An advanced technique to evaluate the electrochromic performances of NiO films by multi-cycle double-step potential chronocoulometry, J. Electrochem. Soc. 163 (2016) H1033–H1040.
[36] S. Xie, Z. Bi, Y. Chen, X. He, X. Guo, X. Gao, X. Li, Electrodeposited Mo-doped $WO_3$ film with large optical modulation and high areal capacitance toward electrochromic energy-storage applications, Appl. Surf. Sci. 459 (2018) 774–781.
[37] K.R. Li, Y.L. Shao, S.Y. Liu, Q.H. Zhang, H.Z. Wang, Y.G. Li, R.B. Kaner, Aluminum-ion-intercalation supercapacitors with ultrahigh areal capacitance and highly enhanced cycling stability: power supply for flexible electrochromic devices, Small 13 (2017) 10.
[38] W.F. Wei, X.W. Cui, W.X. Chen, D.G. Ivey, Improved electrochemical impedance response induced by morphological and structural evolution in nanocrystalline $MnO_2$ electrodes, Electrochim. Acta 54 (2009) 2271–2275.
[39] Y. Li, S. Deng, Y. Chen, J. Gao, J. Zhu, L. Xue, T. Lei, G. Cao, J. Guo, S. Wang, Dual functions of residue Li-reactive coating with $C_4H_6CoO_4$ on high-performance $LiNiO_2$ cathode material, Electrochim. Acta 300 (2019) 26–35.